Ain Shams Engineering Journal xxx (xxxx) xxx

Contents lists available at ScienceDirect

Ain Shams Engineering Journal

journal homepage: www.sciencedirect.com

Full Length Article

Full optoelectronic simulation of all antimony chalcogenide thin film tandem solar cell: Design routes from 4-T to 2-T configuration

Marwa S. Salem [a,b], Ahmed Shaker [c,*], Chao Chen [d], Luying Li [d], Mohamed Abouelatta [e], Arwa N. Aledaily [f], Walid Zein [c], Mohamed Okil [g]

[a] Department of Computer Engineering, College of Computer Science and Engineering, University of Ha'il, Ha'il, Saudi Arabia
[b] Department of Electrical Communication and Electronics Systems Engineering, Faculty of Engineering, Modern Science and Arts University (MSA), Cairo, Egypt
[c] Department of Engineering Physics and Mathematics, Faculty of Engineering, Ain Shams University, Cairo, Egypt
[d] Wuhan National Laboratory for Optoelectronics (WNLO) and School of Optical and Electronic Information, Huazhong University of Science and Technology (HUST), Wuhan, China
[e] Department of Electronics and Communications, Faculty of Engineering, Ain Shams University, Cairo, Egypt
[f] Department of Computer Science and Information, College of Computer Science and Engineering, University of Ha'il, Ha'il, Saudi Arabia
[g] Department of Basic Engineering Sciences, Benha Faculty of Engineering, Benha University, Benha, Egypt

ARTICLE INFO

Keywords:
All-thin-film tandem
Sb_2S_3
Sb_2Se_3
CBO
Current matching
TCAD simulation

ABSTRACT

Antimony chalcogenide, as a newcomer to light harvesting materials, is regarded as an auspicious contender for incorporation as a photoactive layer in thin film tandem solar cells (TFTSCs). The current study introduces the design of all-antimony chalcogenide TFTSC comprised of an Sb_2S_3 (1.7 eV) front subcell and an Sb_2Se_3 (1.2 eV) rear subcell. The challenges to migrating from four-terminal (4-T) to two-terminal (2-T) designs are highlighted and possible solutions are proposed. To commence, a calibration procedure for the two subcells is conducted in alignment with experimental investigations. The benchmarked solar cells yield a power conversion efficiency (PCE) of 8.08 % for the upper subcell and 10.58 % for the lower subcell. Subsequently, upon integration of both subcells within the initial 4-T Sb_2S_3/Sb_2Se_3 TFTSC, the resultant PV cell attains a PCE of 12.27 %. Before transitioning it to a more efficient 2T tandem configuration, we explore alternative inorganic HTL materials to the Spiro-OMeTAD HTL to overcome its practical considerations. Cu_2O is found to be the best HTL alternative to be included for both subcells. Upon stacking into the tandem structure, the combined cell exhibited an efficiency of 15.68 % and a notable J_{sc} of 16.23 mA/cm^2. To further enhance the tandem performance, the device structure is optimized by engineering the CBO of two sub-cells and employing a double ETL design for the front sub-cell. At the considered current matching criterion, the tandem device PCE and J_{sc} are boosted to 27.86 % and 17.60 mA/cm^2, respectively. Based on this full optoelectronic analysis, developed in the Silvaco TCAD environment, a 2-T all antimony chalcogenide tandem configuration can be realized and optimized, paving the way for future experimental endeavors.

1. Introduction

The widespread adoption of Si solar cells has propelled photovoltaic (PV) technology by offering efficient energy conversion [1]. To push Si solar cells further, some novel structures were proposed, including microstructures [2], and nanowires [3]. Additionally, it was shown that the insertion of multiple quantum wells made of $Si_{0.95}Ge_{0.05}$ improves the efficiency by a factor of 1.37 compared to that obtained for conventional Si nanowires [4]. Other studies related to III-V materials solar cells also show advancements, including proposed quantum dot GaAs/GaAsP structures [5]. Nonetheless, thin film solar cells have arisen as a favorable choice, boasting advantages such as flexibility, lightweight design, and cost-effectiveness, setting them apart from their Si and III-V counterparts.

Tandem solar cells, representing a remarkable advancement in PV systems, harness the cumulative power of multiple solar cell layers to capture a broader spectrum of sunlight [6–8]. This tandem approach significantly enhances the overall PCE as compared to single-junction PV cells. In the context of tandem cells, antimony selenide (Sb_2Se_3) and antimony sulfide (Sb_2S_3) materials hold immense prospects as

* Corresponding author.
E-mail address: ahmed.shaker@eng.asu.edu.eg (A. Shaker).

https://doi.org/10.1016/j.asej.2024.102919
Received 14 March 2024; Received in revised form 30 May 2024; Accepted 11 June 2024

candidate photoactive absorbers. Their compelling attributes, incorporating suitable complementary band gaps, high absorption coefficient, abundance in Earth's resources, and remarkable stability, have propelled them into the spotlight as promising candidates for PV technology. Sb_2S_3 demonstrates a bandgap of nearly 1.7 eV [9], while Sb_2Se_3 possesses a bandgap ranging from 1 to 1.2 eV [10]. The bandgaps of Sb_2S_3 and Sb_2Se_3 enable the absorption of incident short and long-wavelength photons from solar radiation. As Sb_2S_3 is characterized by its wide bandgap, it emerges as a proper choice for front subcells in tandem configurations, while Sb_2Se_3 is suitable for rear subcells. Furthermore, the preparation processes of Sb_2S_3 and Sb_2Se_3 are compatible.

The fabrication processes for Sb_2S_3 and Sb_2Se_3 solar cells have undergone significant advancements, enabling the development of efficient tandem devices. A variety of deposition fabrication techniques, such as thermal evaporation, chemical bath deposition, and atomic layer deposition, have been employed to fabricate both Sb_2S_3 and Sb_2Se_3 solar cells [11–14]. These cost-effective methods are remarkably in line with the necessity for economically feasible photovoltaic solutions. Ongoing efforts are directed toward enhancing device efficiency through diverse deposition methods and technological parameter optimizations. Over recent years, dedicated endeavors have been devoted to enhancing the PCEs of Sb_2S_3 and Sb_2Se_3 cells, employing a spectrum of innovative strategies. These strategies encompass interfacial and bandgap engineering techniques, as well as surface passivation, targeting both the carrier transportation layers and the photoactive Sb_2S_3 and Sb_2Se_3 absorbers. Recently, PCEs of 8 % and 10.58 % for Sb_2S_3 and Sb_2Se_3 were reported [15,16]. However, despite these advancements, the PCEs attained are still lower than the Shockley-Queisser (S-Q) limit and notably below than those for CIGS and CdTe thin film cell devices [17]. Research highlights several challenges hindering the achievement of high PCEs for antimony chalcogenide cells, encompassing deep defects, non-ideal series, and shunt resistance, as well as interface and non-radiative recombination. These obstacles significantly impact the open-circuit voltage (*VOC*), contributing to efficiencies falling short of the S-Q limit [18].

The utilization of multijunction technology holds the potential to substantially enhance solar cell performance which enables the solar device to surpass the efficiency limitations set by the S-Q limit for single-junction PV cells. This innovative technology has garnered widespread adoption and application across diverse thin-film cell categories, including thin-film Si, perovskite, and organic solar cells [19–21]. However, limited efforts have been directed towards integrating Sb_2S_3 or Sb_2Se_3 into tandem configurations [22–25]. In [26], a proof-of-concept has been introduced for a tandem device employing Sb_2S_3 and Sb_2Se_3 as the front and rear cell materials, respectively. To enable efficient light transmission to the bottom subcell, graphene was employed as the transparent contact because of its excellent properties including high transparency, conductivity, and charge carrier collection capability. By strategically managing light utilization in the two subcells, a fabricated 4-T tandem cell achieves a remarkable efficiency of 7.93 %.

Practically, the 2-T tandem design may prove unsuitable when stacking Sb_2S_3 and Sb_2Se_3 together during fabrication. One reason for this is that Sb_2Se_3 is susceptible to high-temperature processes during fabrication or annealing, which poses a challenge. Specifically, the Spiro-OMeTAD HTL of the Sb_2Se_3 subcell could be damaged due to the high-temperature requirements, making it incompatible with the Sb_2S_3 subcell. Moreover, an annealing process exceeding 300 °C is necessary after Sb_2Se_3 deposition, potentially causing harm to the Spiro-OMeTAD layer. Furthermore, the utilization of a thin Ag layer as an interlayer to connect the top and bottom subcells may not be appropriate. This is because Ag possesses a large diffusion coefficient and has the potential to react with Sb_2S_3 and Sb_2Se_3 at elevated temperatures. To address these challenges, exploring alternative inorganic HTL materials, such as Cu_2O or WSe_2 and other inorganic candidates, maybe a prudent choice. However, it should be emphasized that NiO, while inorganic, is not a suitable replacement, as it can react with both Sb_2S_3 and Sb_2Se_3 under high-temperature conditions. Thus, in this work, we provide design guidelines for ensuring compatibility in the fabrication processes of 2-T Sb_2S_3/Sb_2Se_3 tandems.

In this paper, we explore the unique attributes of Sb_2S_3 and Sb_2Se_3 as materials for tandem solar cells, shedding light on their design, and performance achievements. Initially, the individual performance of the two subcells is evaluated through calibration versus experimental data [15,16]. Then, the integration of both initial subcells into an Sb_2S_3/Sb_2Se_3 tandem solar cell is studied based on the 4-T configuration. The subsequent investigation delves into 2-T tandem structure optimization, encompassing band offset engineering between the transport and absorber layers for both subcells. The introduced design is based on replacing the organic HTL with inorganic counterparts to alleviate the issues that may appear in fabrication processes, as discussed herein. The influence of electron transportation layer design on TFTSC performance is explored, along with the effect of altering absorber layer thicknesses to attain the highest possible PCE. Notably, the simulation-based approach targets an all-thin-film design, characterized by flexibility that renders it potentially appropriate for applications such as wearable electronics. The simulations are conducted utilizing Silvaco Atlas device simulator package [27], subjecting the solar cells under investigation to AM1.5G illumination (one Sun, 1000 W/m^2).

2. Simulation methodology and device structure

2.1. Silvaco Atlas simulation methodology

In this study, the Silvaco device simulator [6,7,23,24] is utilized for the modeling and simulation of the optical and electrical characteristics of the proposed tandem PV cell. Silvaco TCAD simulation emerges as a powerful tool in accurately modeling tandem solar cells and predicting their performance. Its capability to simulate complex optical and electrical interactions makes it suitable for analyzing the intricate behavior of Sb_2S_3/Sb_2Se_3 tandem solar cells. To ensure the reliability and precision of simulation results, a comprehensive calibration process is employed to correlate the simulated outcomes with experimental data available for Sb_2S_3 and Sb_2Se_3 solar cells of the highest recorded PCEs. This calibration serves as a crucial step in validating the simulation model and enhancing its accuracy for predicting the performance of tandem configurations.

The solution to the equations concerning semiconductor physics is discretized using a designated grid in numerical simulations [28]. Upon employing an illuminated input source, the photogeneration rates are determined and integrated within the generation components of the continuity equation. Within the optical ray-tracing model, employed in the device simulator, the calculation of optical intensity involves utilizing the real component of the refractive index. Conversely, the photogeneration model computes a fresh carrier density through the extinction coefficient. Subsequently, an electrical simulation is utilized to attain the necessary terminal current densities, while the transport characteristics are evaluated based on the drift–diffusion modeling technique.

The selection of the physical models integrated into the device simulator is based on specific criteria. The trap recombination via defect levels within a given layer employs the Shockley-Read-Hall mechanism. Furthermore, recombination in regions of high doping is accounted for by enabling Auger recombination. Additionally, the models of Fermi-Dirac statistics and optical recombination are utilized. In the case of a two-terminal tandem, both subcells necessitate interconnection through a thin tunneling junction or thin interlayers of silver, gold [29], or indium oxide [30]. In this study, an idealized lumped resistance is utilized as a connecting interface between the two subcells to facilitate the flow of current across the subcells [22,23].

Silvaco offers a comprehensive approach to solar cell simulation, capable of modeling the entire tandem structure, providing detailed

optical generation rates by integrating real refractive indices for optical ray tracing and absorption coefficients for photogeneration modeling. This approach allows Silvaco to simulate complex interactions between layers, making it suitable for advanced research and development in solar cell technology. In contrast, other simulation methods like SCAPS operate as 1-dimensional simulators, focusing on simpler simulations of solar cell layers. SCAPS sequentially solves for each layer, starting with the top sub-cell and then moving to the bottom sub-cell using the filtered spectrum from the top layer. In this SCAPS method, simulations are primarily devoted to 4-T solar cell configurations rather than 2-T configurations. Thus, Silvaco's advanced capabilities and integrated modeling techniques provide a more detailed and accurate optoelectronic simulation, making it preferable for cutting-edge research for both 4-T and 2-T tandems.

The main steps undertaken in our study are illustrated in Fig. 1. Initially, two standalone fabricated subcells (Sb_2S_3 and Sb_2Se_3) are calibrated under the illumination of AM1.5G spectrum to ensure accurate characterization, providing a reliable baseline for further simulations and optimizations. Building on this, we construct an initial 4-T tandem cell using Sb_2S_3 for the top cell and Sb_2Se_3 for the bottom cell, serving as a foundation for further refinement. We then propose a 2-T Sb_2S_3/Sb_2Se_3 tandem cell configuration. The proposed 2-T tandem cell undergoes a series of optimization steps, including investigating the conduction band offsets between different materials in the top subcell to improve charge carrier transport and reduce recombination losses, exploring the effects of using single and dual ETLs in the top subcell to enhance electron extraction, and optimizing the absorber thicknesses in both sub-cells to ensure maximum light absorption. The final step in the optimization process is achieving the current matching condition, where the current generated by the top and bottom subcells is matched to maximize the overall PCE.

2.2. Calibration of Sb_2S_3 and Sb_2Se_3 subcells

In this subsection, we will highlight both device structures of Sb_2S_3 and Sb_2Se_3 cells that are used to form the tandem device. Our approach involves the use of experimental solar cells, with a wide bandgap Sb_2S_3 [15] and a narrow bandgap Sb_2Se_3 cell [16]. The n-i-p Sb_2S_3 heterostructure involves the layers FTO/CdS/Sb_2S_3/Spiro-OMeTAD/Au, with a schematic representation displayed in Fig. 2**(a)**. The primary material parameters of the various layers are addressed in Table 1. The CdS and Spiro-OMeTAD layers are applied as electron and hole transportation layers (ETL and HTL), respectively, while FTO and Au are utilized as front and back electrodes. We assume that the carrier type of Sb_2S_3 is p-type, having an acceptor density of 1×10^{14} cm^{-3} [22,31]. Defect concentrations in the Sb_2S_3 film are obtained from an experimental study [15], while interfacial defects at ETL/Sb_2S_3 and HTL/Sb_2S_3 interfaces are considered neutral. Table 2 exhibits the main defects parameters of Sb_2S_3 as well as at the interfaces. The values of the work functions of the top FTO and back Au electrodes are 4.73 eV and 5.1 eV [7].

The external quantum efficiency (*EQE*) and the current–voltage (*J-V*) characteristic curves under illumination of fabricated and simulated Sb_2S_3 devices are depicted in Fig. 2**(b) and (c)** using the given parameters. The simulated PV cell shows $J_{sc} = 17.18$ mA/cm^2, $V_{oc} = 0.759$ V, $FF = 61.95$ %, and $PCE = 8.08$ %, which closely match the reported parameters as revealed in Table 3, thereby justifying the simulation model within the Atlas simulator. It is noteworthy to highlight that the elevated recombination rates within the devices arising from defects at the CdS/Sb_2S_3 interface and trap sites in Sb_2S_3 contribute to the lower *VOC*. As a result, it becomes imperative to optimize the appropriate ETL along with absorber critical parameters for enhanced performance.

In addition, the n-i-p structured bottom Sb_2Se_3 PV cell is constructed using a solar cell that is fabricated through the FTO/CdS/Sb_2Se_3/Spiro-OMeTAD/Au configuration [16], as seen in Fig. 3**(a)**. The primary cell parameters are derived from experimental findings, such as the

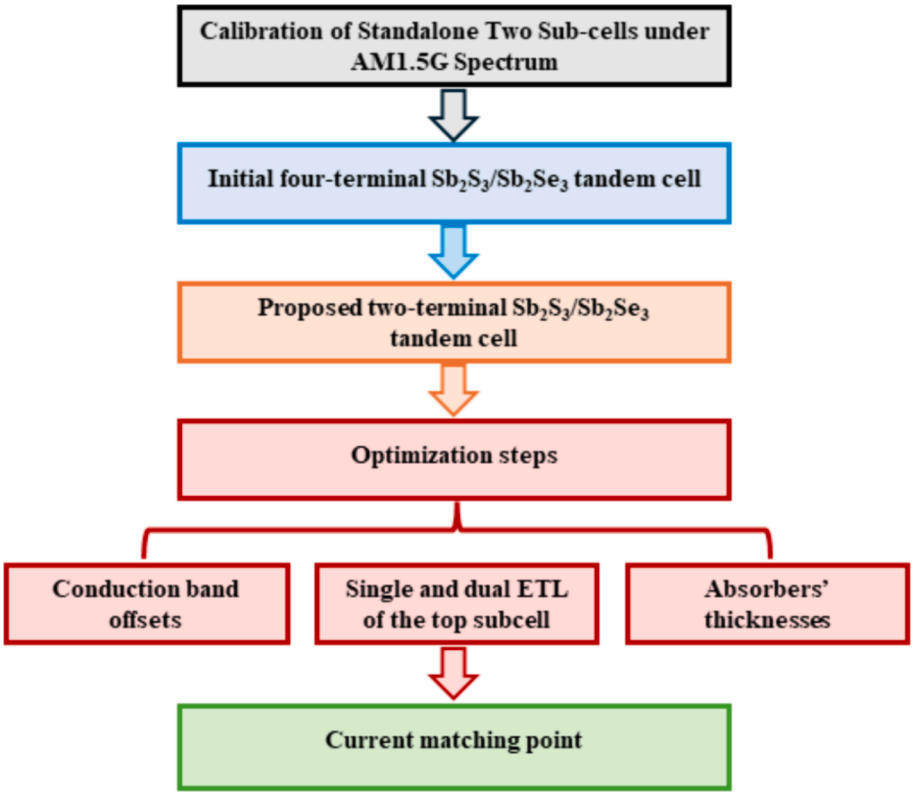

Fig. 1. Flowchart summarizing the workflow steps performed in our simulation work.

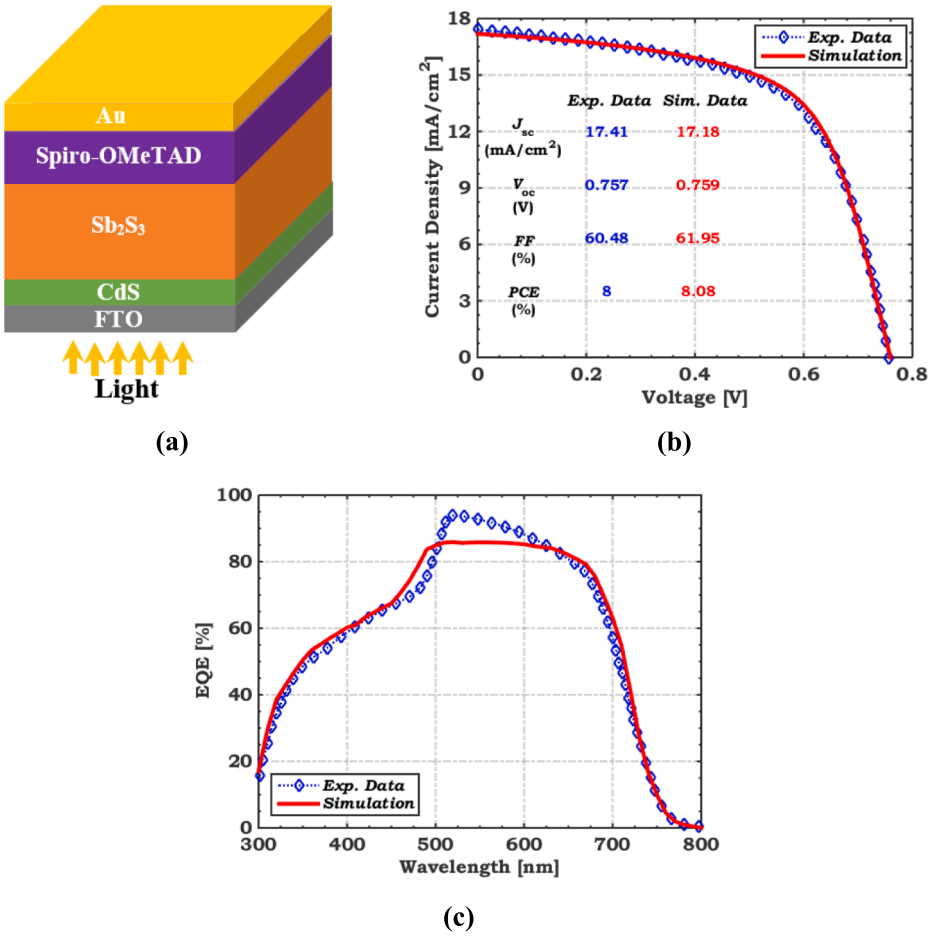

Fig. 2. Sb_2S_3 top cell: (a) Basic cell arrangement, (b) J–V, and (c) EQE curves of simulation vs experimental data [15] under AM1.5G one-Sun illumination.

Table 1
Main factors of various layers of Sb_2S_3 and Sb_2Se_3 solar cells.

Parameters	CdS	Sb_2S_3	Sb_2Se_3	Spiro-OMeTAD
Thickness, t (nm)	t_{Top} = 50 t_{Bot} = 60	310	275	t_{Top} = 50 t_{Bot} = 150
Energy gap, E_g (eV)	2.4	1.72	1.2	3.17
Electron affinity, χ (eV)	4.2	3.70	4.13	2.05
Relative permittivity, ε_r	10	7	10	3
Electron/Hole mobility, μ_n/μ_p (cm^2/Vs)	100/25	0.8/0.2	5/1.5	2×10^{-4}/2×10^{-4}
DOS in conduction band /valence band, N_c/N_v (cm^{-3})	2.2×10^{18} /1.9×10^{19}	3×10^{19} /7×10^{19}	2.2×10^{18} /1.8×10^{19}	2.2×10^{18} /1.8×10^{19}
Donor density, N_D (cm^{-3})	1×10^{17}	–	–	–
Acceptor density, N_A (cm^{-3})	–	1×10^{14}	6.5×10^{15}	2×10^{19}
Reference	[37]	[15,22]	[38]	[39]

thicknesses, doping concentration, conduction and valence energy edges, and semiconductor bulk defects of the photoactive Sb_2Se_3 layer [16]. The technological factors of CdS, Spiro-OMeTAD, and Sb_2Se_3 are exhibited in Table 1. The defect density within the Sb_2Se_3 absorber and at the interfaces are also documented in Table 2. The *J–V* and *EQE* characteristic curves of fabricated and simulated Sb_2Se_3 solar devices [16] are displayed in Fig. 3**(b) and (c)**, applying the given factors. Notably, the measured J_{SC} obtained from the *EQE* spectrum is 30.71 mA/cm^2 which is comparatively less than J_{SC} found from the *J–V* characteristics (33.52 mA/cm^2). This discrepancy in J_{SC} values between the *EQE*-extracted and *J–V* curve has been previously highlighted in research of Sb_2Se_3 PV cells [32,33]. According to the relevant literature [33,34], the phenomenon may be ascribed to the presence of deep levels in the junction region that serve as centers for both generation and recombination. In instances where light levels are low (as in *EQE* measurement), photogenerated carriers may recombine at these centers. Conversely, high light intensity (specifically for AM1.5G at 1000 W/m^2) may cause some of these centers to be filled as a result of photoexcitation by sub-bandgap photons. Consequently, the measured J_{SC} at AM1.5G illuminated source may yield a significantly higher value than the integrated current from *EQE* acquired under the condition of low-intensity and monochromatic radiation. To appropriately align with the experimental *EQE* data, the absorption coefficient of the Sb_2Se_3 absorber layer can be adjusted, as demonstrated in Fig. 3**(c)**. The simulated photovoltaic parameters correspond with the measured data, as shown in Table 3, signifying the justification of the Silvaco Atlas simulation. To further substantiate the accuracy of the model, the relationship between V_{OC} and light intensity (I) created from simulation versus measured data [16] is presented in Fig. 3**(d)**. In this figure, the constant ε represents the proportionality constant relating V_{OC} and ln(I), where V_{OC} and I are related by [35,36],

$$V_{OC} = \varepsilon V_T \ln(I) + \text{constant} \quad (1)$$

3. Results and discussions

3.1. 4-Terminal tandem cell

The configuration of the initial 4-T tandem cell of Sb_2S_3 top subcell and Sb_2Se_3 bottom subcell is shown in Fig. 4**(a)**. In this structure, the

Table 2
Defects parameters in Sb_2S_3 and Sb_2Se_3 cells and at the interfaces.

Parameters	Bulk defects			Interface defects			
	Sb_2S_3		Sb_2Se_3	ETL/Sb_2S_3	Sb_2S_3/HTL	ETL/Sb_2Se_3	Sb_2Se_3/HTL
Defect type	donor	donor	acceptor	neutral	neutral	neutral	neutral
Carrier capture cross-section (cm^2)	1.24×10^{-17}	6.59×10^{-16}	3.3×10^{-15}	1×10^{-15}	1×10^{-15}	1×10^{-15}	1×10^{-15}
Energy level above E_v (eV)	0.50	0.78	0.60	0.85	0.85	0.6	0.6
Concentration (N_t) (cm^{-3})	1.85×10^{13}	1.57×10^{14}	1×10^{13}	1×10^{15}	1×10^{15}	2.5×10^{13}	2.5×10^{13}
Ref.	[15]	[15]	[16]	[22]	[22]	[16]	[16]

Table 3
PV metrics of simulated and experimental Sb_2S_3 and Sb_2Se_3 solar cells.

PV Metrics		J_{sc} (mA/cm^2)	V_{oc} (V)	*FF* (%)	*PCE* (%)
Sb_2S_3 PV cell	Experimental [15]	17.41	0.757	60.48	8
	This work	17.18	0.759	61.95	8.08
Sb_2Se_3 PV cell	Experimental [16]	33.52	0.467	67.64	10.57
	This work	33.55	0.467	67.59	10.58

calibrated cells are used as the main subcells, while graphene electrode is employed as a back contact for the front subcell. Fig. 4**(b)** displays the *J–V* curves of subcell components of the 4-T tandem device. The segmented spectral absorption between both subcells is illustrated in Fig. 4**(c)**, which shows the external quantum efficiency of Sb_2S_3 and Sb_2Se_3 in tandem. Regarding the PV metrics of the 4-T tandem, recorded values for the top, rear and tandem cells are listed in Table 4. The top and bottom subcells reached a PCE of 8.05 % and 4.22 % with a V_{OC} of 0.76 V and 0.432, respectively. The PCE of the 4-T tandem device is thus just 12.27 %. Notably, this 4-T tandem design cannot be converted to 2-T configuration for the practical considerations discussed therebefore. Thus, to migrate from 4-T to 2-T tandem devices, the organic HTL will be replaced by inorganic materials in order to insure the feasibility of the design for possible future fabrication.

3.2. Proposed 2-Terminal tandem cell

In the previous subsection, the two subcells were initially designed with an organic HTL using Spiro-OMeTAD. In our study, we undertook a redesign of this tandem cell, transitioning it to a more efficient 2-T tandem configuration. This redesign can be achieved by substituting the Spiro-OMeTAD HTL with various inorganic alternatives, such as CuSCN, CuI, and Cu_2O. The chosen inorganic materials are expected to boost the performance and stability of the tandem device. The basic physical parameters of these HTL materials are documented in Table 5.

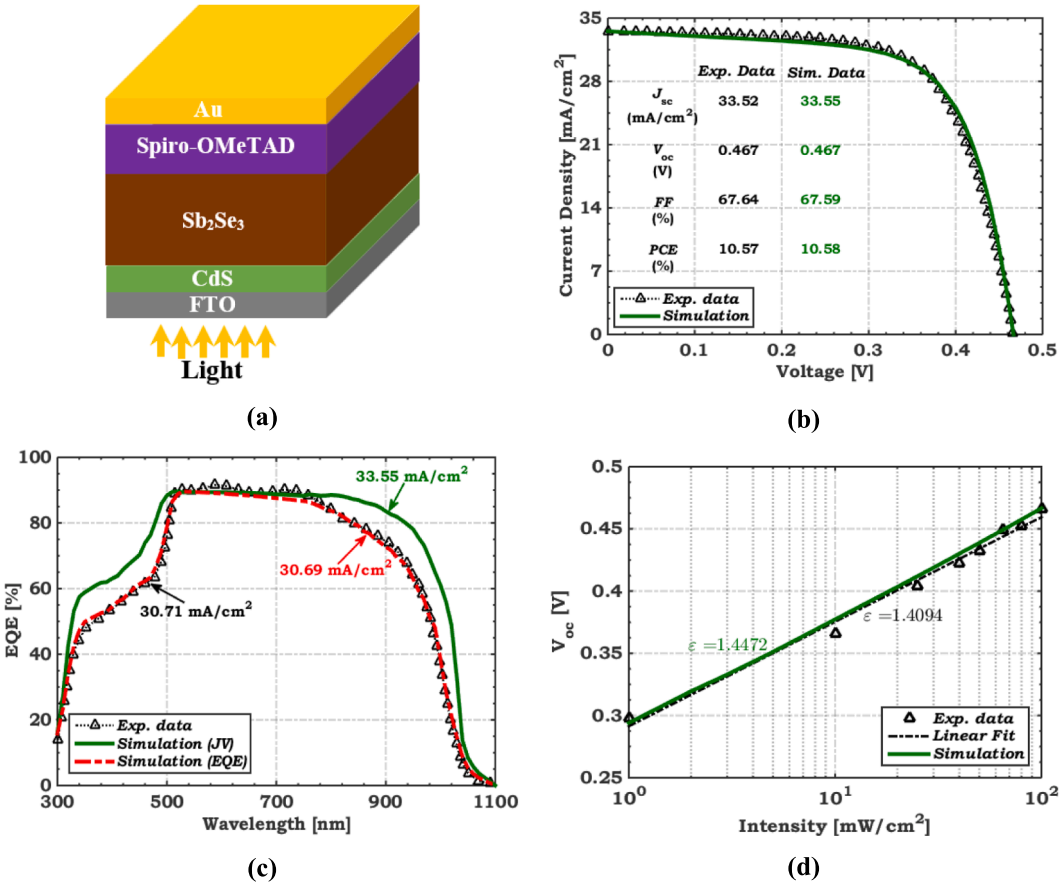

Fig. 3. Sb_2Se_3 bottom cell: (a) Basic cell arrangement, (b) J–V, (c) EQE and (d) V_{oc} vs I curves of simulation against experimental data [16] under AM1.5G one-Sun illumination.

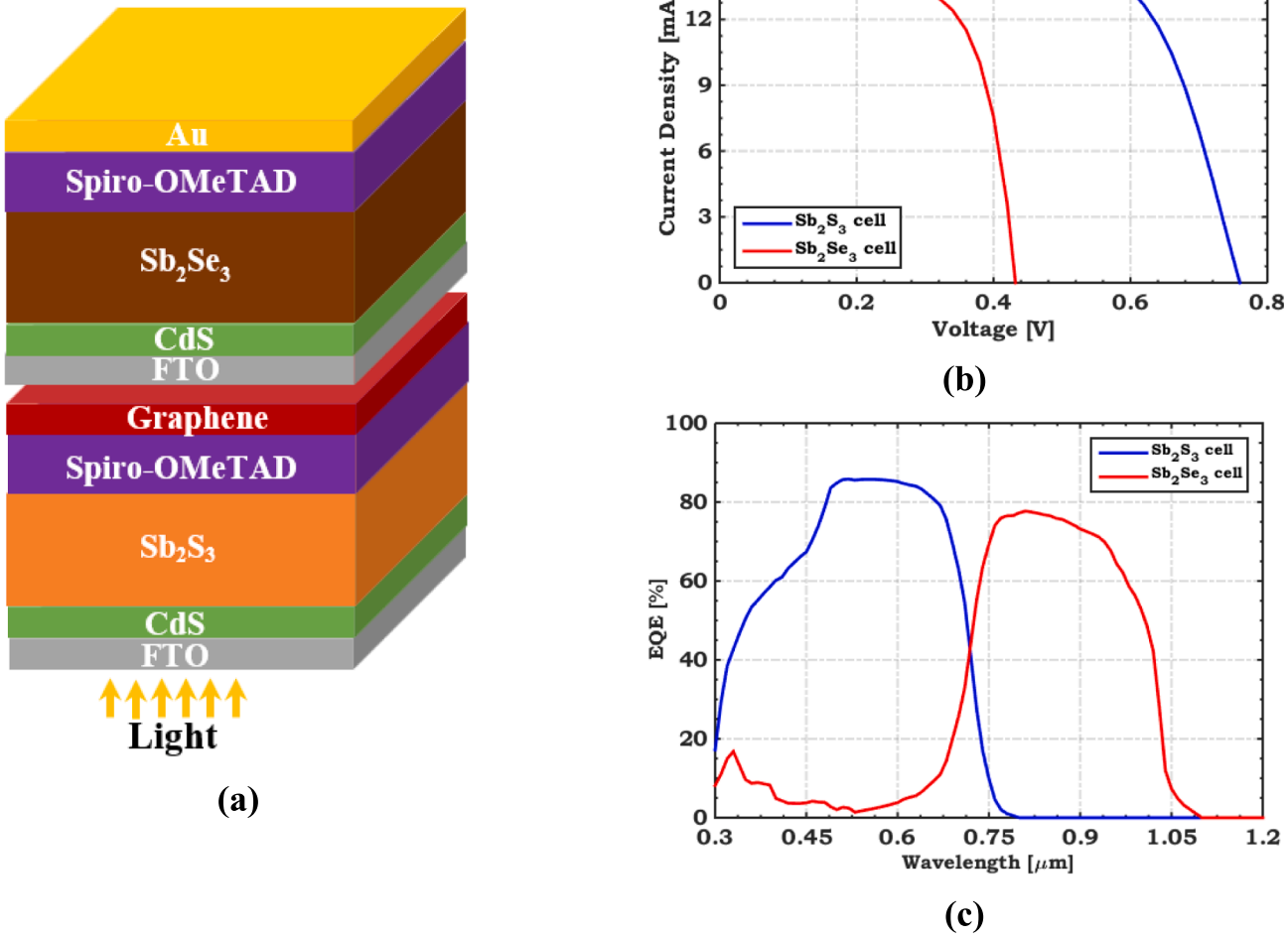

Fig. 4. **(a)** Schematic illustration showing key layers, **(b)** *J–V*, and **(c)** *EQE* curves of 4-terminal Sb_2S_3/Sb_2Se_3 tandem cell.

Table 4
PV metrics of 4-Terminal Sb_2S_3 and Sb_2Se_3 subcells.

PV Metrics	J_{sc} (mA/cm^2)	V_{oc} (V)	*FF* (%)	*PCE* (%)
Top Sb_2S_3 subcell	17.18	0.760	61.70	8.05
Bottom Sb_2Se_3 subcell	14.20	0.432	68.85	4.22
Tandem cell	–	–	–	12.27

Following the replacement of Spiro-OMeTAD, we meticulously characterized both subcells performance by simulating the *J–V* characteristics and extracting the corresponding optoelectronic factors, that are exhibited in Table 6 (for Sb_2S_3) and Table 7 (for Sb_2Se_3). According to these results, it can be concluded that Cu_2O achieves the highest efficiency for both front and rear subcells.

Now, the structure for the proposed 2-T Sb_2S_3/Sb_2Se_3 tandem cell is presented, as shown in Fig. 5**(a)**. After utilizing the tandem simulation by incorporating the initial parameters of the constituting cells, the outcomes are presented in Fig. 5**(b) and (c)**, which depict the *J–V* curves and *EQE* spectra, respectively. The relevant PV factors are: $J_{sc} = 16.23$ mA/cm^2, $V_{oc} = 1.36$ V, $FF = 71.11$, and $PCE = 15.68$ %. Notably, the V_{oc} (1.36 V) of the TFTSC is almost the same as the sum of the V_{oc} of the standalone subcells (0.736 and 0.621 V), whereas its current is restricted by that of the Sb_2S_3 top cell, which is 16.04 mA/cm^2. As indicated in Fig. 5**(b)**, the photocurrent of the Sb_2S_3 subcell presented a strong bias dependence. The distinctly generated photocurrents in the subcells possess a negative bias across the subcell with a lesser photocurrent because of the extra photocurrent in the neighboring subcell [42]. This

Table 5
Fundamental physical factors of various inorganic HTL materials.

Parameters	CuSCN	CuI	Cu_2O
t (nm)	50	50	50
E_g (eV)	3.6	3.1	2.17
χ (eV)	1.7	2.1	3.2
ε_r	10	6.5	10
μ_n/μ_p (cm^2/Vs)	100/25	100/43.9	200/80
N_c	2.2×10^{19}	2.8×10^{19}	2×10^{17}
$/N_v$ (cm^{-3})	$/1.8 \times 10^{18}$	$/1 \times 10^{19}$	$/1.1 \times 10^{19}$
Reference	[40]	[6]	[41]

Table 6
Band and PV parameters for Sb_2S_3 cell with various HTL materials.

HTL	VBO	J_{sc} (mA/cm^2)	V_{oc} (V)	*FF* (%)	*PCE* (%)
Spiro-OMeTAD (initial)	−0.20	17.18	0.759	61.95	8.08
Cu_2O	**−0.05**	**17.38**	**0.757**	**63.09**	**8.30**
CuSCN	−0.12	17.28	0.757	63.03	8.24
CuI	−0.22	17.21	0.760	61.88	8.09

Table 7
Band and PV parameters for Sb_2Se_3 cell with various HTL materials.

HTL	VBO	J_{sc} (mA/cm^2)	V_{oc} (V)	*FF* (%)	*PCE* (%)
Spiro-OMeTAD (initial)	−0.11	33.55	0.467	67.59	10.58
Cu_2O	**0.04**	**33.35**	**0.469**	**67.70**	**10.59**
CuSCN	−0.03	33.27	0.469	67.70	10.56
CuI	−0.13	33.26	0.470	67.77	10.58

negative bias would raise the photocurrent from 16.04 to 16.23 mA/cm^2.

3.3. 2-T tandem optimization

In this subsection, we will be focusing on the optimization steps that can be applied to the 2-T Sb_2S_3/Sb_2Se_3 tandem cell. The subsection is divided into four separate parts. In the first part, we examine the impact that the CBO has on the performance of the two subcells. In addition, the concept of a double ETL is explored to enhance the tandem performance in the second part. Finally, we will take a closer look at the effect that different absorber thicknesses have on tandem performance, and we will be assessing the current matching point (CMP) for the highest conversion efficiency in the last two parts.

A. Conduction band offset of two subcells

Given that the PCE of the PV cell hinges on the discernment of the ETL, which is chiefly determined by its energetic and transportation attributes such as carrier mobilities and band alignment, a well-matched ETL can substantially curtail interface recombination. Attaining an ideal conduction band offset (CBO) necessitates precise band alignment at the interface between the ETL and absorber [43]. The CBO holds pivotal significance in determining both V_{oc} and overall cell efficiency, and it can be defined as,

$$CBO = \Delta E_c = \chi_{absorber} - \chi_{ETL} \quad (2)$$

Three possible scenarios for band alignment exist at any heterojunction interface. The first involves a cliff-like band offset with a negative CBO value, followed by a second condition where positive CBO values spike-like band offset are confronted. Lastly, a flat band state emerges as the third potential scenario, characterized by a zero CBO. It is widely acknowledged that cliff-like band offsets at the interface result in pronounced interfacial recombination [44]. Moreover, significant spike-like band offsets, indicating CBOs exceeding 0.3 eV, can impede interface carrier transfer [44]. Generally, in the context of thin film PV cells, slight spike-like or flat band offsets are considered more favorable [45].

Here, the CBO impact of front and bottom subcells is systematically examined. In a theoretical investigation, the bottom CBO is altered from −0.2 to 0.5 eV, while the top CBO is varied from −0.6 to 0.4 eV. The change in the tandem efficiency is displayed in Fig. 6**(a)**. Based on this simulation run, the maximum PCE is achieved within the range of 0.25 to 0.4 for the bottom CBO and −0.1 to −0.5 for the top CBO. To accomplish the CBO design values, we propose $Cd_{1-x}Zn_xS$ as an ETL material because of its electron affinity and bandgap tunability. The

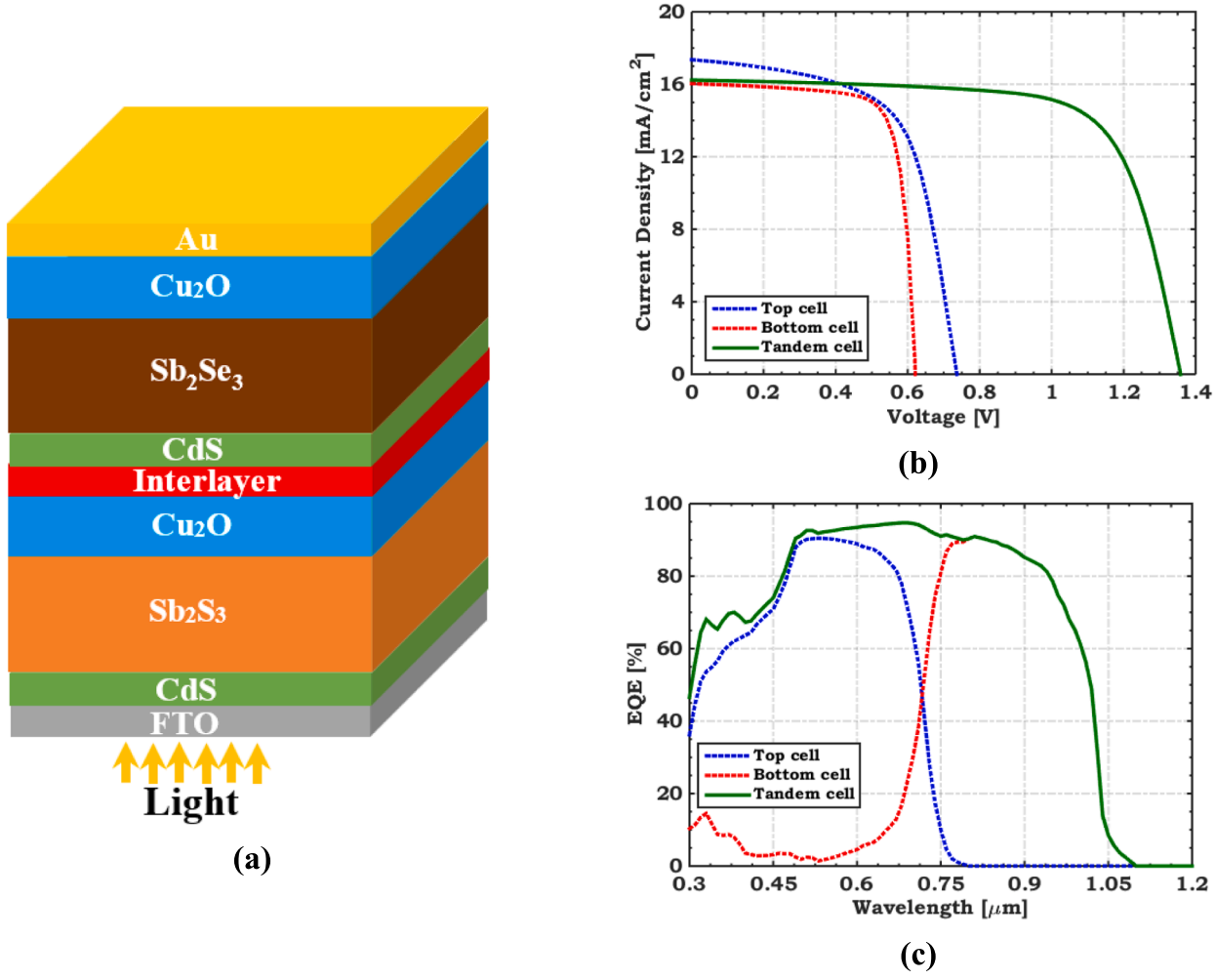

Fig. 5. **(a)** Schematic illustration showing main layers, **(b)** *J–V*, and **(c)** *EQE* curves of proposed 2T Sb_2S_3/Sb_2Se_3 tandem cell.

changes in bandgap energy and electron affinity of $Cd_{1-x}Zn_xS$ as a function of Zn content were acquired from existing literature [46], as portrayed in Fig. 6**(b)**. In addition, Fig. 6**(c)** presents the variation of the CBO of the two subcells, depending on the variation of Zn content. Based on the CBO design values, $Cd_{0.4}Zn_{0.6}S$ is an appropriate material for use as ETL in both subcells. Here, the PV metrics are J_{sc} = 16.77 mA/ cm^2, V_{oc} = 1.71 V, *FF* = 78.10 %, and an efficiency of 22.36 %.

B. ETL Design Configuration for Top Subcell

Advancing the performance of PV devices is greatly facilitated by improving charge collection and separation. With regard to this, the ETL performs a decisive role. Consequently, the exploration of a dual ETL concept is undertaken here to enhance tandem operation. This strategy involves employing two distinct materials as a substitution to a single ETL, aiming to overcome limitations envisioned in conventional designs. Numerous experimental reports have been published that evaluate the application of dual ETL arrangements in boosting the PCE and stability of thin film solar devices [47–52]. By incorporating two different ETL materials, the objective is to optimize charge transportation, minimize recombination losses, and consequently achieve superior overall performance.

Here, we investigate the combination of a dual ETL architecture comprising a 50 nm thick $Cd_{0.9}Zn_{0.1}S$ layer as a neighboring film to the FTO, along with a 50 nm thick $Cd_{0.4}Zn_{0.6}S$ layer. The difference in energy between the work function of the FTO contact and the LUMO of the first ETL ($Cd_{0.9}Zn_{0.1}S$) is well-tailored (Φ_F = 0.46 eV). Additionally, the difference in energy between the LUMO of the second ETL ($Cd_{0.4}Zn_{0.6}S$) and that of the photoactive layer is adjusted to be sufficiently low (CBO = -0.15 eV) to ease the transfer of electrons. The resulting output metrics include J_{sc} = 16.69 mA/cm^2, V_{oc} = 1.99 V, FF = 82.30 %, and PCE = 27.33 %. Therefore, the dual ETL design proves to enhance cell performance and achieve higher efficiency. The use of $Cd_{0.9}Zn_{0.1}S/Cd_{0.4}Zn_{0.6}S$ as a dual ETL in the present design results in a substantial percentage increase of 22.23 % compared to the single ETL tandem cell.

To interpret the performance trends with single and dual ETL configurations, energy band diagrams are plotted for three different cases: a single ETL employing CdS and $Cd_{0.4}Zn_{0.6}S$, and a dual ETL using $Cd_{0.9}Zn_{0.1}S/Cd_{0.4}Zn_{0.6}S$, as depicted in Fig. 7. From Fig. 7**(a)**, it can be deduced that although $Cd_{0.4}Zn_{0.6}S$ exhibits satisfactory alignment with the absorber film, its misalignment with the front electrode provides a larger barrier height that impedes electrons' transmission. In contrast, Fig. 7**(b)** demonstrates that utilizing two ETLs establishes a satisfactory band alignment with the front electrode, creating a lower barrier height that enhances electron transportation to the contact while simultaneously offering hole-blocking abilities. Further, Fig. 8 illustrates the *J–V* characteristics (for AM1.5G illumination) regarding several top ETL structures.

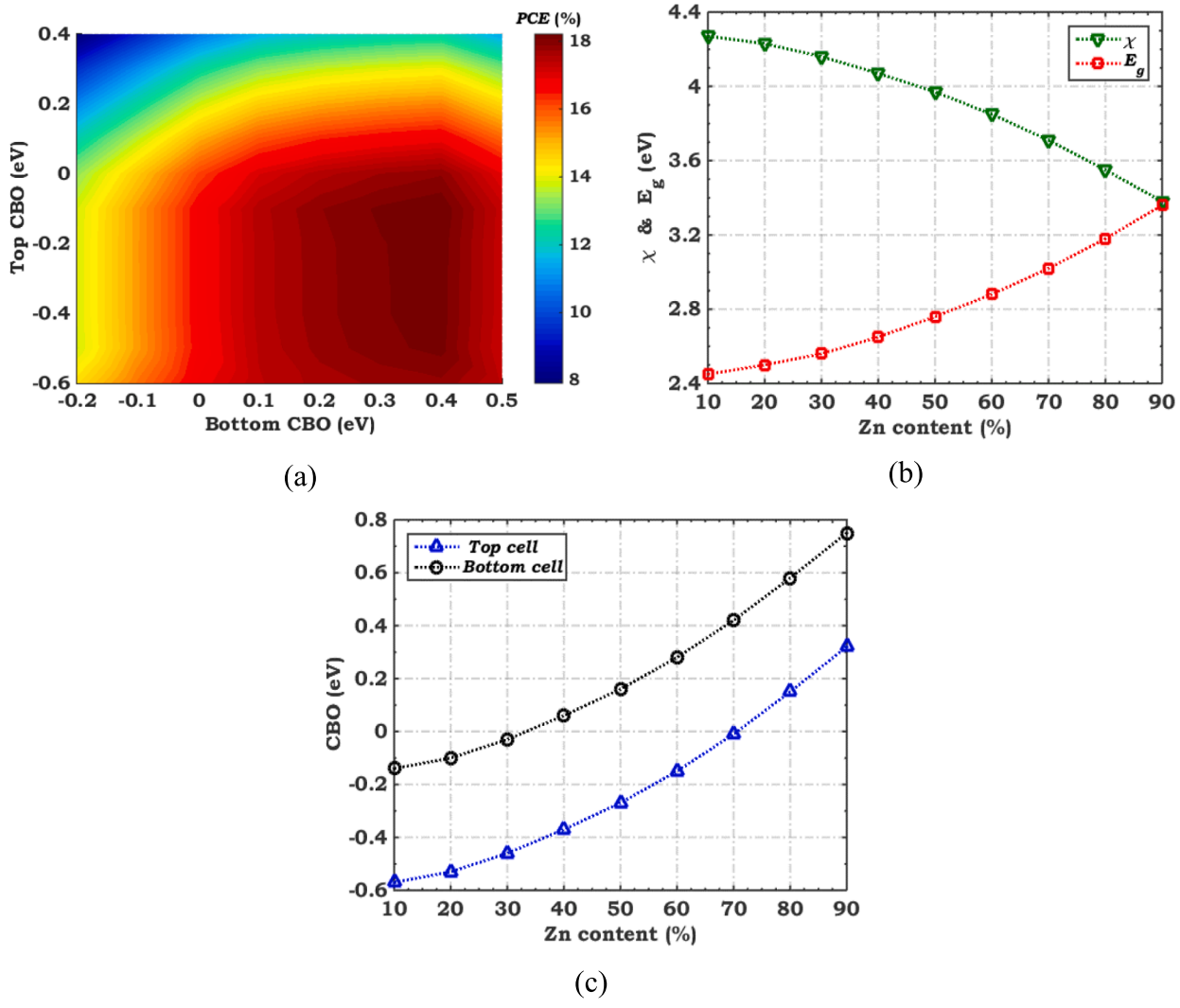

Fig. 6. (a) Contour plot of the tandem PCE at various CBO in the top and bottom device, (b) Change in E_g and χ of $Cd_{1-x}Zn_xS$ dependent on Zn content variation, and (c) Variation in two subcells CBO of $Cd_{1-x}Zn_xS$ depending on the change in Zn content.

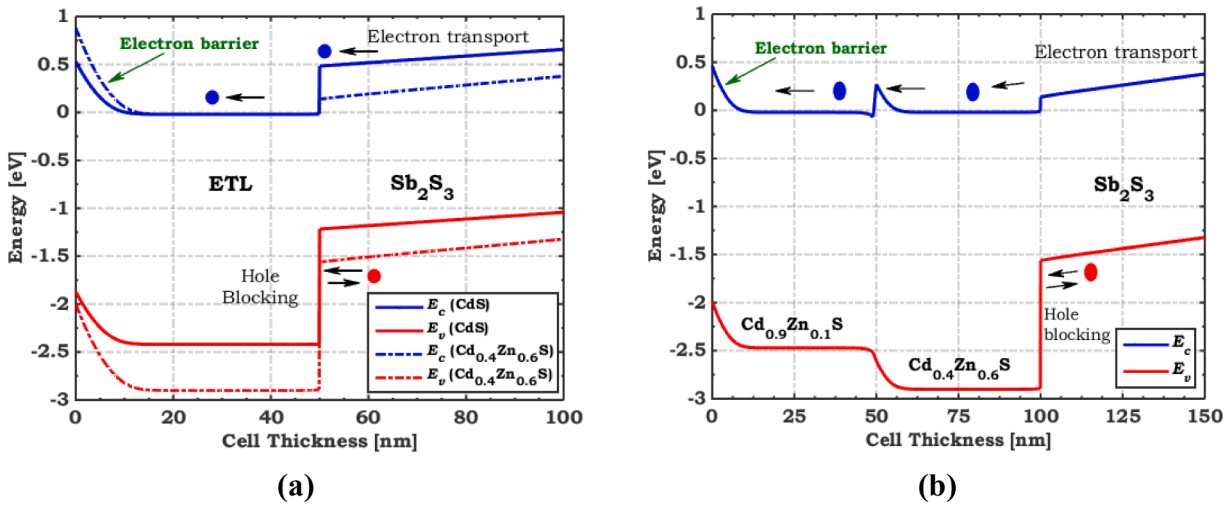

Fig. 7. Energy band profiles (drawn at dark conditions) for Sb_2S_3/Sb_2Se_3 tandem with various top ETL architectures (a) single ETL (CdS and $Cd_{0.4}Zn_{0.6}S$) and (b) dual ETL ($Cd_{0.9}Zn_{0.1}S$ /$Cd_{0.4}Zn_{0.6}S$).

C. Impact of Thicknesses of Photoactive Layers

Fig. 9 illustrates how the PCE of the tandem is impacted by variations in the thickness of the top and bottom absorber layers. Specifically, the thickness of the front Sb_2S_3 absorber (t_{TA}) ranges from 100 to 600 nm, while that of the rear Sb_2Se_3 layer (t_{BA}) varies from 200 to 500 nm. The findings indicate that increasing t_{BA} from 200 to 500 nm has no substantial impact on PCE, provided t_{TA} remains below 200 nm. However, as t_{TA} falls below 200 nm, *PCE* steadily drops from 25.25 % to 19 %. The most effective combination of thickness is determined to be 400 nm for t_{TA} and 500 nm for t_{BA}, which results in a *PCE* of 28.20 %. However, in order to conserve materials and save cost, it is decided to select thicknesses of 375 nm for the front absorber and 400 nm for the rear absorber, as increasing the thickness of the bottom absorber beyond 400 nm does not significantly improve PCE. The output metrics for these choices are $J_{sc} = 17.28$ mA/cm^2, $V_{oc} = 1.99$ V, $FF = 81.58$ %, and an efficiency of 28 %. It is clear that the *PCE* accomplished by $t_{TA} = 375$ nm and $t_{BA} = 400$ nm is very close to the optimal *PCE* value.

D. Current Matching Point (CMP)

Herein, the possibility of CMP is examined by altering t_{TA} values

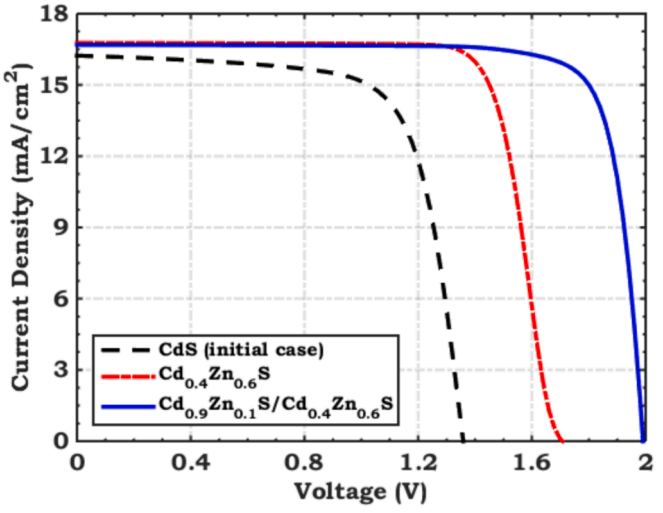

Fig. 8. Illuminated *J–V* characteristic curves of Sb_2S_3/Sb_2Se_3 TFTSC with various top ETL configurations.

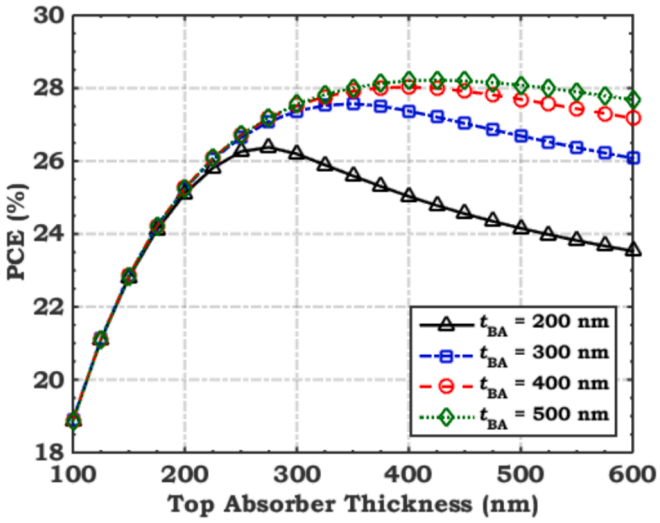

Fig. 9. The dependence of tandem PCE on the thickness of front and rear active films.

within the range of 280 to 400 nm while keeping t_{BA} constant at 400 nm. Fig. 10**(a)** demonstrates the correlation between J_{sc} and the t_{TA} of both subcells. As t_{TA} increases, the top subcell absorbs more photons and less light is transferred to the bottom subcell, resulting in an increase in J_{sc} for the front subcell while a reduction in J_{sc} is observed for the rear subcell, as depicted in Fig. 10**(a)**. A CMP is observed at $J_{sc} = 17.60$ mA/cm^2 and $t_{TA} = 338$ nm. The tandem device is modeled under these conditions and the *J–V* output curves for the tandem and its constituent subcells are demonstrated in Fig. 10**(b)**. The correlated metrics are shown in Table 8. The tandem demonstrates a maximum J_{sc} of 17.60 mA/cm^2 with a V_{oc} of 1.99 V with an efficiency of 27.86 %. The V_{oc} of 1.99 V is the result of the top and bottom subcells' voltages (1.17 V, and 0.82 V, respectively), indicating that the two subcells are working effectively together at the recombination junction. Furthermore, Fig. 10 **(c)** illustrates the *EQE* spectra of the tandem and subcells at the CMP.

3.4. Comparison between initial and optimized 2-T tandem designs

In a given tandem, the individual top and bottom subcells can be further characterized by the analytical two-diode model to gain some physical insights into the recombination mechanisms occurring in each

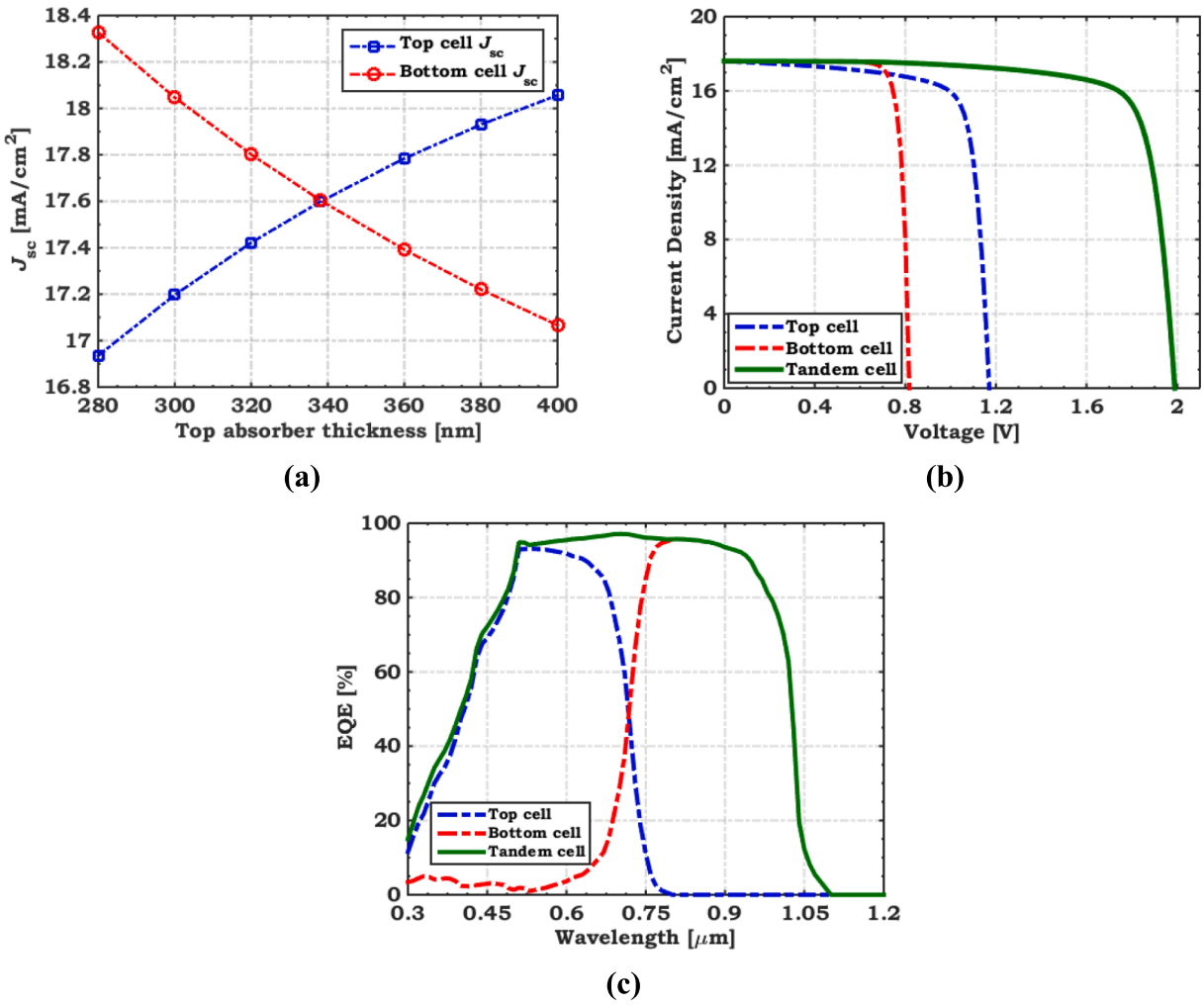

Fig. 10. (a) J_{sc} of subcells versus top absorber thickness. (b) *J-V* characteristics and (c) *EQE* spectra of the tandem device and corresponding subcells under CMP.

Table 8
Two-diode model parameters along with PV metrics for top cell and rear cell for the initial and optimized 2-T Sb_2S_3/Sb_2Se_3 tandems.

	Cell	J_L (mA/cm^2)	J_{01} (A/cm^2)	J_{02} (A/cm^2)	R_s (Ω·cm^2)	R_p (Ω·cm^2)	J_{sc} (mA/cm^2)	V_{oc} (V)	*FF* (%)	*PCE* (%)
Initial tandem	Top	17.711	2.71×10^{-20}	9.05×10^{-9}	3.51	298.1	17.36	0.736	62.71	8.02
	Bottom	16.064	3.55×10^{-13}	2.14×10^{-8}	0.172	934.3	16.04	0.621	76.85	7.65
Optimized tandem	Top	17.772	1.53×10^{-22}	8.49×10^{-13}	1.956	840.8	17.60	1.17	77.78	16.01
	Bottom	17.597	2.23×10^{-16}	2.91×10^{-10}	0.099	5.3×10^5	17.60	0.82	84.58	12.17

subcell. The two-diode model has been extensively utilized to outline the illuminated and dark *J-V* characteristics of various types of solar cells [53]. The analytical equation describing a typical two-diode model is,

$$J = J_L - J_{o1}\exp\left(\frac{V+JR_s}{V_T}\right) - J_{o2}\exp\left(\frac{V+JR_s}{2V_T}\right) + \frac{V+JR_s}{R_p} \quad (3)$$

here, J_L is the photogenerated current density and V_T is the thermal voltage. The series and shunt resistance are denoted by R_s and R_p, respectively, where R_s reflects the internal resistance impact, while R_p signifies the extent of leakage current. In this equation, the first diode is characterized by an ideality factor (n) of 1, while the second diode has an ideality factor of 2. In the case of $n = 1$, the SRH recombination usually takes place in the bulk region, where electron and hole concentrations differ substantially. On the other hand, for the case of $n = 2$, the SRH recombination takes place in the depletion region, where electron and hole concentrations are comparable. In this context, the reverse saturation current J_{o1} is an indication of the degree of bulk recombination, while J_{o2} represents the degree of depletion recombination under the high injection scenario. Thus, J_{o1} or J_{o2} is manipulated as a sign of the SRH recombination under low or high injection conditions, respectively [53].

After applying Equation (3), we can determine the equivalent circuit parameters (J_L, J_{o1}, J_{o2}, R_s and R_p) for each subcell. The *J-V* curves, shown in Fig. 11**(a)** and Fig. 11**(b)** for the top and bottom subcells respectively, depict both the initial and optimized (at CMP) tandem cases. These figures demonstrate a good agreement between the fitting curves of the equivalent two-diode model and the TCAD solutions. The extracted parameters of the two-diode model for both subcells are presented in Table 8, which also includes the main PV parameters of the cells derived from the TCAD simulations. For the top cell, there is a noticeable reduction in R_s and an increase in R_p in the optimized case compared to the initial one. Additionally, recombination losses are significantly reduced, as indicated by the decreases in J_{o1} and J_{o2}.

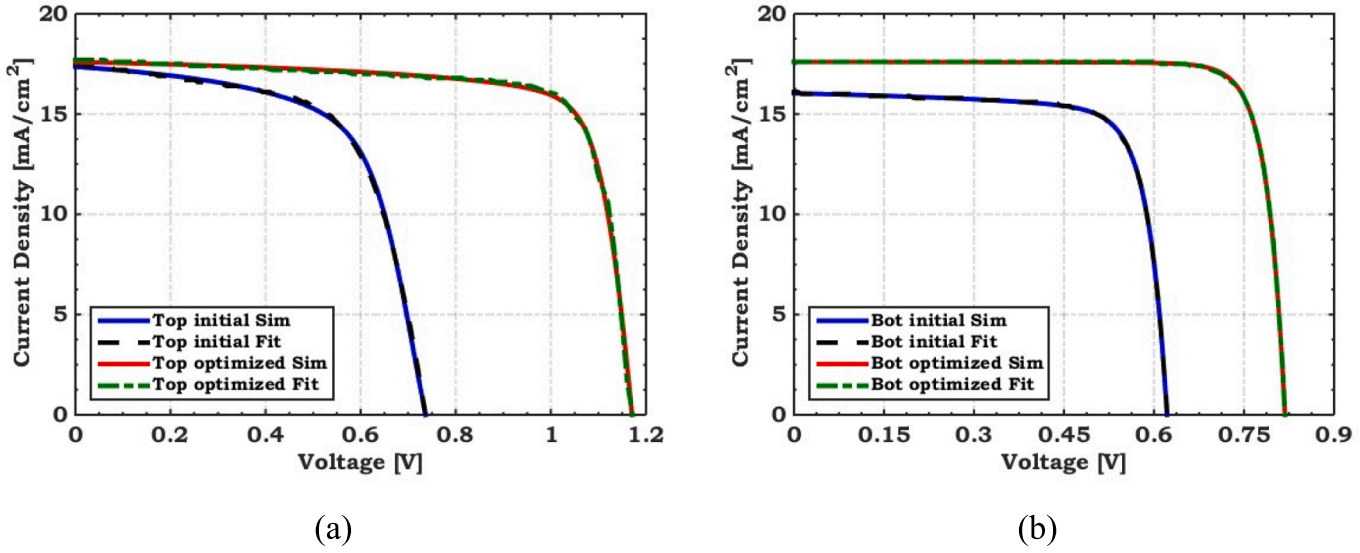

Fig. 11. Illuminated *J–V* characteristics of the individual subcells for the initial and optimized 2-T Sb_2S_3/Sb_2Se_3 tandems, comparing both TCAD simulation and analytical two-diode model fit: (a) top subcell and (b) bottom subcell.

Similarly, for the bottom cell, significant reductions in J_{o1}, J_{o2}, and R_s, along with a significant increase in R_p, can be observed. These results confirm the improvements in both subcells, as evidenced by the *J-V* curves in Fig. 11.

Another important factor that can quantitatively highlight sources of losses in a solar cell is the fill factor, which is typically influenced by non-radiative and resistive losses [54]. The non-radiative loss component of the fill factor can be identified by [54],

$$\Delta FF_{non-rad} = FF_{S-Q} - FF_o(V_{OC}) \tag{4}$$

where $FF_{S\text{-}Q}$ is the S-Q fill factor limit, at a given bandgap, while FF_o is the fill factor value without resistive losses. The FF_o can be calculated from the empirical equation [55],

$$FF_o(V_{OC}) \approx \left[\frac{V_{OC}}{V_T} - \ln\left(\frac{V_{OC}}{V_T} + 0.72\right)\right] / \left(\frac{V_{OC}}{V_T} + 1\right) \tag{5}$$

Additionally, the resistive loss part of the fill factor can be formulated by [54],

$$\Delta FF_{res} = FF_o(V_{OC}) - FF \tag{6}$$

where *FF* is the fill factor resulting from simulations in our case. For the top and bottom subcells, having $E_g = 1.72$ eV and $E_g = 1.2$ eV, the FF_{SQ} is 91.11 % and 87.76 %, respectively. Based on the calculations of *FF* (given in Table 8), and FF_o (from equation (5)), the coefficients $\Delta FF_{non\text{-}rad}$ and ΔFF_{res} can be computed. Fig. 12 illustrates the non-radiative and resistive *FF* loss components for both the top and bottom subcells in the initial and optimized tandem configurations. As depicted in the figure, both non-radiative and resistive losses are significantly reduced in both subcells after optimization. This reduction is more pronounced in the bottom cell, indicating a greater improvement in its performance. Thus, the successfully optimized tandem design effectively mitigates the loss mechanisms, leading to enhanced overall efficiency.

3.5. State-of-the-art comparison

Finally, a comparative analysis of our optimized tandem cell with other TFTSC contenders is presented, as illustrated in Table 9. The table displays a mix of experimental and numerically computed tandem cells. Among the reported tandem cells, antimony chalcogenide tandem cell has undergone experimental testing and attained a *PCE* of 7.93 % for a 4 T structure [26]. Also, a 4-T $Sb_2(S,Se)_3$/Si tandem device was fabricated,

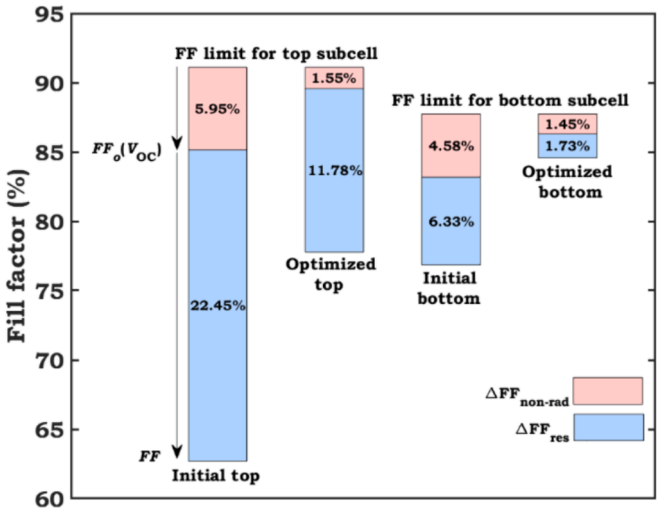

Fig. 12. Detailed FF losses of top and bottom subcells in the initial and optimized 2-T Sb_2S_3/Sb_2Se_3 tandems.

and an overall PCE of 11.66 % was reported [56]. Theoretical research has suggested that a triple-junction all-antimony chalcogenide TFTSC can achieve a high PCE of around 33 % [57].

Little effort has been devoted to the 2-T antimony chalcogenide tandem design. Recently, Hajjiah presented an investigation on a tandem solar cell using Sb_2S_3 and Sb_2Se_3 as the absorber layers with energy gaps of 1.7 eV and 1.2 eV, respectively. The device characteristics, radiative recombination, and optimum thickness of this tandem cell were analyzed using filtered spectrum analysis and current-matching techniques in COMSOL. The optimized tandem cell achieved a PCE of 14.66 %, with the Sb_2S_3 and Sb_2Se_3 subcells having 350 nm and 760 nm thicknesses, respectively [58]. In addition, Shrivastav et al. introduced a 2 T tandem that pairs a top Sb_2S_3 subcell with a bottom Sb_2Se_3 subcell, with a recombination junction formed by a thin ITO film. The optimized tandem cell achieved a PCE of 14 % [31]. Besides, Dahmardeh et al. investigated incorporating Sb_2S_3/Sb_2Se_3 in a 2-T tandem structure, reaching a PCE of 22.2 %, having thicknesses of 420 nm and 1020 nm for the Sb_2S_3 and Sb_2Se_3 subcells, respectively [59].

Moreover, Sb_2Se_3 material has been used in various studies as the

Table 9
A state-of-the-art comparative analysis between optoelectronic metrics of Sb_2S_3/Sb_2Se_3 tandem cell and other tandem cells acknowledged in the literature.

Materials	Tandem connection	Approach	J_{sc} (mA/cm^2)	V_{oc} (V)	*FF* (%)	*PCE* (%)	REF.
Sb_2S_3/Sb_2Se_3	4T	Exp.	–	–	–	7.93	[26]
$Sb_2(S,Se)_3$/Si	4T	Exp.	–	–	–	11.66	[56]
Perovskite/Sb_2Se_3	4T	Exp.	–	–	–	20.58	[25]
$Sb_2S_3/Sb_2(S_{0.7}Se_{0.3})_3/Sb_2Se_3$	2T	Sim.	11.08	3.44	86.49	32.98	[57]
Sb_2S_3/Si	2T	Sim.	18.04	1.64	82.41	24.34	[22]
Sb_2S_3/Si	4T	Sim.	–	–	–	29.26	[60]
Sb_2S_3/Si	2T	Sim.	19.17	1.91	82.48	30.22	[60]
All-polymer/Sb_2Se_3	2T	Sim.	15.40	2.02	77.75	24.24	[24]
Organic/Sb_2Se_3	2T	Sim.	17.03	1.68	74.86	21.52	[23]
Sb_2S_3/Sb_2Se_3	2T	Sim.	15.50	1.58	56.90	14	[31]
Sb_2S_3/Sb_2Se_3	2T	Sim.	16.32	1.48	60.70	14.66	[58]
Sb_2S_3/Sb_2Se_3	2T	Sim.	20.15	1.02	59.58	22.20	[59]
Sb_2S_3/Sb_2Se_3	2T	Sim.	17.60	1.99	79.60	27.86	This work

bottom cell material for 2-T and 4-T tandem cells. Lately, Cai et al. demonstrated the first perovskite/Sb_2Se_3 4-T tandem solar cell with a specially designed and fabricated transparent electrode to optimize spectral response. The final optimized 4-T tandem achieved an impressive efficiency of 20.58 % [25]. In simulation studies, 2-T tandems such as all-polymer/Sb_2Se_3 and organic/Sb_2Se_3 have been analyzed using Silvaco tools [23,24], achieving PCEs of over 20 %. On the other hand, Sb_2S_3 material has been used in various simulation studies as the top cell material for 2-T and 4-T Sb_2S_3/Si tandem cells. The simulated PCEs of these studies reached 30 %, using SCAPS [60] and Silvaco [22].

The PCE of our optimized 2-T tandem reached a remarkable value above 27 % by just optimizing the carrier transport layers without incorporating reducing defects. Based on these findings, our simulation of the suggested tandem cell exhibits positive traits such as a high *PCE* and V_{OC}, indicating that our design could be suitable for all-thin-film tandems. More importantly, the introduced design paves the way to transfer 4-T all-antimony chalcogenide tandems into 2-T configurations based on practical prospects, paving the way for further enhancements related to technology constraints.

It should be highlighted here that while TCAD simulations provide valuable insights into the behavior of Sb_2S_3/Sb_2Se_3 tandem solar cells, they have limitations related to idealized assumptions and material variability. For instance, TCAD simulations often rely on idealized device structures and uniform material properties. In reality, the fabrication processes of tandem solar cells introduce variability in material properties, layer thicknesses, and interface quality, which may not be fully accounted for in simulations. This can lead to inaccuracies in predicting device performance. Additionally, in our simulations, an ideal interlayer between the two sub-cells is assumed, which may not accurately represent the actual device behavior. Moreover, the ray tracing optical model used in our simulations does not account for interference or diffraction effects, which may not fully capture the accurate optical behavior inside the various layers of the tandem.

4. Conclusions

In conclusion, this paper has extensively explored the potential of antimony chalcogenide materials as promising candidates for tandem solar cell technology. Their non-toxic and abundant nature, combined with elevated absorption coefficients in the visible range, positions them as attractive absorber materials. The study focused on a transferring 4-T to 2-T tandem configuration, comprising an Sb_2S_3 top subcell and as Sb_2Se_3 bottom subcell, taking fabrication constraints into account. The research began by individually assessing the performance of these subcells, demonstrating a PCE of 8.08 % for the front cell and 10.58 % for the rear cell. Then, the calibrated subcells were used in an initial 4T-tandem cell achieving a PCE of 12.27 %. To obtain an efficient 2T tandem configuration, two subcells were redesigned by substituting the Spiro-OMeTAD HTL with various inorganic alternatives. It was found that Cu_2O is the best HTL alternative for both subcells. Upon integration into the tandem structure, the combined cell exhibited a power efficiency of 15.68 % and a notable J_{sc} of 16.23 mA/cm^2.

To further enhance PCE, numerous design proposals are targeted. The issue of band alignment is systematically investigated and controlled by engineering the CBO of two subcells and incorporating a dual ETL arrangement for the front subcell. In addition, the thicknesses optimization of the Sb_2S_3 and Sb_2Se_3 absorber films was evaluated, followed by the design of the CMP. The maximum efficiency was attained for a Sb_2S_3 and Sb_2Se_3 thicknesses of 338 nm and 400 nm, respectively. For this tandem design, the optoelectronic metrics are: J_{sc} = 17.60 mA/cm^2, V_{oc} = 1.99 V, FF = 79.60 %, and an overall efficiency of 27.86 %.

CRediT authorship contribution statement

Marwa S. Salem: Writing – review & editing, Writing – original draft, Visualization, Validation, Software, Methodology, Conceptualization. **Ahmed Shaker:** Writing – review & editing, Writing – original draft, Visualization, Validation, Supervision, Methodology, Conceptualization. **Chao Chen:** Writing – review & editing, Visualization, Supervision, Methodology, Investigation, Conceptualization. **Luying Li:** Writing – review & editing, Supervision, Methodology, Investigation, Conceptualization. **Mohamed Abouelatta:** Writing – review & editing, Visualization, Validation, Software, Methodology, Investigation, Formal analysis. **Arwa N. Aledaily:** Writing – original draft, Software, Methodology, Conceptualization. **Walid Zein:** Validation, Software, Methodology, Investigation. **Mohamed Okil:** Writing – review & editing, Visualization, Validation, Software, Methodology, Investigation, Formal analysis.

Declaration of Competing Interest

The authors declare that they have no known competing financial interests or personal relationships that could have appeared to influence the work reported in this paper.

Acknowledgement

This research has been funded by Scientific Research Deanship at University of Ha'il - Saudi Arabia through project number <<RG-23 069>>.

References

[1] Okil M, Salem MS, Abdolkader TM, Shaker A. From crystalline to low-cost silicon-based solar cells : a review. Silicon 2022;14:1895–911. https://doi.org/10.1007/s12633-021-01032-4.
[2] Salem MS, Zekry A, Shaker A, Abouelatta M, Abdolkader TM. Performance enhancement of a proposed solar cell microstructure based on heavily doped

silicon wafers. Semicond Sci Technol 2019;34:035012. https://doi.org/10.1088/1361-6641/ab0078.
[3] Sahoo MK, Kale P. Integration of silicon nanowires in solar cell structure for efficiency enhancement: a review. J Mater 2019;5:34–48. https://doi.org/10.1016/j.jmat.2018.11.007.
[4] Safi M, Aissat A, Guesmi H, Vilcot JP. SiGe quantum wells implementation in Si based nanowires for solar cells applications. Dig J Nanomater Biostruct 2023;18:327–42. https://doi.org/10.15251/DJNB.2023.181.327.
[5] Guesmi H, Aissat A, Safi M, Berbezier I. Efficiency improvement of GaAs Quantum Dot in $GaAs_{1-x}P_x$ matrix for solar cell applications. Microelectronics J 2020;99:104738. https://doi.org/10.1016/j.mejo.2020.104738.
[6] Alanazi TI, Eid OI, Okil M. Numerical study of flexible perovskite/Si tandem solar cell using TCAD simulation. Opt Quantum Electron 2023;55:1152. https://doi.org/10.1007/s11082-023-05320-8.
[7] Okil M, Shaker A, Ahmed IS, Abdolkader TM, Salem MS. Evaluation of a proposed barium di-silicide tandem solar cell using TCAD numerical simulation. Opt Quantum Electron 2023;55:475. https://doi.org/10.1007/s11082-023-04734-8.
[8] Alanazi TI, El Sabbagh M. Proposal and design of flexible all-polymer/CIGS tandem solar cell. Polymers (Basel) 2023;15:1823. https://doi.org/10.3390/polym15081823.
[9] Kondrotas R, Chen C, Tang J. Sb_2S_3 solar cells. Joule 2018;2:857–78. https://doi.org/10.1016/j.joule.2018.04.003.
[10] Chen C, Li K, Tang J. Ten years of Sb_2Se_3 thin film solar cells. Sol RRL 2022;6:2200094. https://doi.org/10.1002/solr.202200094.
[11] Zhang L, Wu K, Yu J, Yu Y, Wei Y. Sb_2Se_3 films fabricated by thermal evaporation and post annealing. Vacuum 2021;183:109840. https://doi.org/10.1016/j.vacuum.2020.109840.
[12] Haidar F, Pradel A, Chen Y, Record M-C. Deposition of Sb_2Se_3 thin films on Pt substrate via electro-chemical atomic layer epitaxy (EC-ALE). J Electroanal Chem 2020;879:114774. https://doi.org/10.1016/j.jelechem.2020.114774.
[13] Pan G, Wang D, Gao S, Gao P, Sun Q, Liu X, et al. Substrate structured Sb_2S_3 thin film solar cells fabricated by rapid thermal evaporation method. Sol Energy 2019;182:64–71. https://doi.org/10.1016/j.solener.2019.02.014.
[14] Chalapathi U, Poornaprakash B, Ahn C-H, Park S-H. Rapid growth of Sb_2S_3 thin films by chemical bath deposition with ethylenediamine tetraacetic acid additive. Appl Surf Sci 2018;451:272–9. https://doi.org/10.1016/j.apsusc.2018.04.249.
[15] Wang S, Zhao Y, Che B, Li C, Chen X, Tang R, et al. A novel multi-sulfur source collaborative chemical bath deposition technology enables 8%-efficiency Sb_2S_3 planar solar cells. Adv Mater 2022;34:1–10. https://doi.org/10.1002/adma.202206242.
[16] Zhao Y, Wang S, Li C, Che B, Chen X, Chen H, et al. Regulating deposition kinetics via a novel additive-assisted chemical bath deposition technology enables fabrication of 10.57%-efficiency Sb_2Se_3 solar cells. Energy Environ Sci 2022;15:5118–28. https://doi.org/10.1039/d2ee02261c.
[17] Nayak PK, Mahesh S, Snaith HJ, Cahen D. Photovoltaic solar cell technologies: analysing the state of the art. Nat Rev Mater 2019;4:269–85. https://doi.org/10.1038/s41578-019-0097-0.
[18] Chen C, Tang J. Open-circuit voltage loss of antimony chalcogenide solar cells: status origin, and possible solutions. ACS Energy Lett 2020;5:2294–304. https://doi.org/10.1021/acsenergylett.0c00940.
[19] Lehr J, Langenhorst M, Schmager R, Gota F, Kirner S, Lemmer U, et al. Energy yield of bifacial textured perovskite/silicon tandem photovoltaic modules. Sol Energy Mater Sol Cells 2020;208:110367. https://doi.org/10.1016/j.solmat.2019.110367.
[20] Bahro D, Koppitz M, Colsmann A. Tandem organic solar cells revisited. Nat Photon 2016;10:354–5. https://doi.org/10.1038/nphoton.2016.96.
[21] Cao Y, Zhu X, Tong X, Zhou J, Ni J, Zhang J, et al. Ultrathin microcrystalline hydrogenated Si/Ge alloyed tandem solar cells towards full solar spectrum conversion. Front Chem Sci Eng 2020;14:997–1005. https://doi.org/10.1007/s11705-019-1906-0.
[22] Okil M, Shaker A, Ahmed IS, Abdolkader TM, Salem MS. Design and analysis of Sb_2S_3/Si thin film tandem solar cell. Sol Energy Mater Sol Cells 2023;253:112210. https://doi.org/10.1016/j.solmat.2023.112210.
[23] Alanazi TI, Alanazi A, Touti E, Agwa AM, Kraiem H, Alanazi M, et al. Proposal and numerical analysis of organic/Sb_2Se_3 all-thin-film tandem solar cell. Polymers (Basel) 2023;15:2578. https://doi.org/10.3390/polym15112578.
[24] Alanazi TI, Shaker A, Gad M, Okil M. Optimization of all-polymer/Sb_2Se_3 tandem solar cells for enhanced efficiency: a comprehensive TCAD modeling approach. Phys Scr 2024;99:065516. https://doi.org/10.1088/1402-4896/ad4315.
[25] Cai Z, Sun J, Cai H, Gu Y, Tang R, Zhu C, et al. Sb_2Se_3 as a bottom cell material for efficient perovskite/Sb_2Se_3 tandem solar cells. Energy Mater Devices 2024;2:9370027. https://doi.org/10.26599/EMD.2024.9370027.
[26] Zhang J, Lian W, Yin Y, Wang X, Tang R, Qian C, et al. All antimony chalcogenide tandem solar cell. Sol RRL 2020;4:2000048. https://doi.org/10.1002/solr.202000048.
[27] Atlas User's Manual, Silvaco Inc., Santa Clara, USA, (n.d.). https://silvaco.com/products/tcad/device_simulation/atlas/atlas.html (accessed September 1, 2023).
[28] S. Michael, A.D. Bates, M.S. Green, Silvaco atlas as a solar cell modeling tool, in: Conf. Rec. IEEE Photovolt. Spec. Conf., 2005: pp. 719–721. doi: 10.1109/pvsc.2005.1488232.
[29] Chen X, Jia Z, Chen Z, Jiang T, Bai L, Tao F, et al. Efficient and reproducible monolithic perovskite/organic tandem solar cells with low-loss interconnecting layers. Joule 2020;4:1594–606. https://doi.org/10.1016/j.joule.2020.06.006.
[30] Brinkmann KO, Becker T, Zimmermann F, Kreusel C, Gahlmann T, Theisen M, et al. Perovskite–organic tandem solar cells with indium oxide interconnect. Nature 2022;604:280–6. https://doi.org/10.1038/s41586-022-04455-0.
[31] Shrivastav N, Yadav V, Bhattarai S, Madan J, Hossain MK, Samajdar DP, et al. Two-terminal tandem solar cell with Sb_2S_3/Sb_2Se_3 absorber pair: achieving 14% power conversion efficiency. Phys Scr 2023;98:115110. https://doi.org/10.1088/1402-4896/ad000e.
[32] Liu D, Tang R, Ma Y, Jiang C, Lian W, Li G, et al. Direct hydrothermal deposition of antimony triselenide films for efficient planar heterojunction solar cells. ACS Appl Mater Interf 2021;13:18856–64. https://doi.org/10.1021/acsami.1c02393.
[33] Amin A, Li D, Duan X, Vijayaraghavan SN, Menon HG, Wall J, et al. Enhanced efficiency and stability in Sb_2S_3 seed layer buffered Sb_2Se_3 solar cells. Adv Mater Interf 2022;9:2200547. https://doi.org/10.1002/admi.202200547.
[34] Hegedus SS, Shafarman WN. Thin-film solar cells: device measurements and analysis. Prog Photovoltaics Res Appl 2004;12:155–76. https://doi.org/10.1002/pip.518.
[35] Zhang H, Cheng J, Lin F, He H, Mao J, Wong KS, et al. Pinhole-free and surface-nanostructured niox film by room-Temperature solution process for high-performance flexible perovskite solar cells with good stability and reproducibility. ACS Nano 2016;10:1503–11. https://doi.org/10.1021/acsnano.5b07043.
[36] Salem MS, Okil M, Shaker A, Albaker A, Alturki M. Design of n-i-p and p-i-n Sb_2Se_3 solar cells: role of band alignment. J Phys Energy 2023;5:045007. https://doi.org/10.1088/2515-7655/acf688.
[37] Salah MM, Hassan KM, Abouelatta M, Shaker A. A comparative study of different ETMs in perovskite solar cell with inorganic copper iodide as HTM. Optik (Stuttg) 2019;178:958–63. https://doi.org/10.1016/j.ijleo.2018.10.052.
[38] Salem MS, Shaker A, Abouelatta M, Alanazi A, Al-Dhlan KA, Almurayziq TS. Numerical analysis of hole transport layer-free antimony selenide solar cells: Possible routes for efficiency promotion. Opt Mater (Amst) 2022;129:112473. https://doi.org/10.1016/j.optmat.2022.112473.
[39] Gamal N, Sedky SH, Shaker A, Fedawy M. Design of lead-free perovskite solar cell using $Zn_{1-x}Mg_xO$ as ETL: SCAPS device simulation. Optik (Stuttg) 2021;242:167306. https://doi.org/10.1016/j.ijleo.2021.167306.
[40] Hossain MK, Rubel MHK, Toki GFI, Alam I, Rahman MF, Bencherif H. Effect of various electron and hole transport layers on the performance of $CsPbI_3$ -based perovskite solar cells: a numerical investigation in DFT, SCAPS-1D, and wxAMPS frameworks. ACS Omega 2022;7:43210–30. https://doi.org/10.1021/acsomega.2c05912.
[41] Li S, Cao Y-L, Li W-H, Bo Z-S. A brief review of hole transporting materials commonly used in perovskite solar cells. Rare Met 2021;40:2712–29. https://doi.org/10.1007/s12598-020-01691-z.
[42] Gharibshahian I, Sharbati S, Orouji AA. Design of $CuIn_{1-y}Ga_ySe_2$/$Si_{1-x}Ge_x$ Tandem solar cells with controlled current matching. IET Optoelectron 2020;14:199–209. https://doi.org/10.1049/iet-opt.2019.0060.
[43] Minemoto T, Murata M. Theoretical analysis on effect of band offsets in perovskite solar cells. Sol Energy Mater Sol Cells 2015;133:8–14. https://doi.org/10.1016/j.solmat.2014.10.036.
[44] Scheer R, Schock HW. Chalcogenide photovoltaics: physics, technologies, and thin film devices. John Wiley & Sons 2011. https://doi.org/10.1002/9783527633708.
[45] Chen C, Liu X, Li K, Lu S, Wang S, Li S, et al. High-efficient Sb_2Se_3 solar cell using $Zn_xCd_{1-x}S$ n-type layer. Appl Phys Lett 2021;118:172103. https://doi.org/10.1063/5.0030430.
[46] Salem MS, Shaker A, Almurayziq TS, Alshammari MT. Prospective efficiency boosting of full-inorganic single-junction $Sb_2(S, Se)_3$ solar cell. Sol Energy Mater Sol Cells 2022;248:112001. https://doi.org/10.1016/j.solmat.2022.112001.
[47] Yi H, Wang D, Mahmud MA, Haque F, Upama MB, Xu C, et al. Bilayer SnO_2 as electron transport layer for highly efficient perovskite solar cells. ACS Appl Energy Mater 2018;1:6027–39. https://doi.org/10.1021/acsaem.8b01076.
[48] Pitchaiya S, Eswaramoorthy N, Natarajan M, Santhanam A, Ramakrishnan VM, Asokan V, et al. Interfacing green synthesized flake like-ZnO with TiO_2 for bilayer electron extraction in perovskite solar cells. New J Chem 2020;44:8422–33. https://doi.org/10.1039/d0nj01559h.
[49] Li N, Yan J, Ai Y, Jiang E, Lin L, Shou C, et al. A low-temperature TiO_2/SnO_2 electron transport layer for high-performance planar perovskite solar cells. Sci China Mater 2020;63:207–15. https://doi.org/10.1007/s40843-019-9586-x.
[50] Otoufi MK, Ranjbar M, Kermanpur A, Taghavinia N, Minbashi M, Forouzandeh M, et al. Enhanced performance of planar perovskite solar cells using TiO_2/SnO_2 and TiO_2/WO_3 bilayer structures: roles of the interfacial layers. Sol Energy 2020;208:697–707. https://doi.org/10.1016/j.solener.2020.08.035.
[51] Zhao Y, Li C, Niu J, Zhi Z, Chen G, Gong J, et al. Xiao, Zinc-based electron transport materials for over 9.6%-efficient S-rich $Sb_2(S, Se)_3$ solar cells. J Mater Chem A 2021;9:12644–51. https://doi.org/10.1039/D1TA02356J.
[52] Lachore WL, Andoshe DM, Mekonnen MA, Hone FG. Recent progress in electron transport bilayer for efficient and low-cost perovskite solar cells: a review. J Solid State Electrochem 2022;26:295–311. https://doi.org/10.1007/s10008-021-05064-z.
[53] Zeng Y, Ding Z, Liu Z, Liu W, Liao M, Yang X, et al. Efficiency-loss analysis of monolithic perovskite/silicon tandem solar cells by identifying the patterns of a dual two-diode model's current-voltage curves. J Semicond 2023;44:082702. https://doi.org/10.1088/1674-4926/44/8/082702.
[54] Tian J, Zhang K, Xie Z, Peng Z, Zhang J, Osvet A, et al. Quantifying the energy losses in $CsPbI_2Br$ perovskite solar cells with an open-circuit voltage of up to 1.45 V. ACS Energy Lett 2022;7:4071–80. https://doi.org/10.1021/acsenergylett.2c01883.
[55] Guillemoles J-F, Kirchartz T, Cahen D, Rau U. Guide for the perplexed to the shockley-queisser model for solar cells. Nat Photonics 2019;13:501–5. https://doi.org/10.1038/s41566-019-0479-2.

[56] Qian C, Sun K, Cong J, Cai H, Huang J, Li C, et al. Bifacial and Semitransparent $Sb_2(S, Se)_3$ Solar cells for single-junction and tandem photovoltaic applications. Adv Mater 2023;35:2303936. https://doi.org/10.1002/adma.202303936.
[57] Cao Y, Liu C, Jiang J, Zhu X, Zhou J, Ni J, et al. Theoretical insight into high-efficiency triple-junction tandem solar cells via the band engineering of antimony chalcogenides. Sol RRL 2021;5:2000800. https://doi.org/10.1002/solr.202000800.
[58] Hajjiah A. Modeling a tandem solar cell based on Sb_2S_3 and Sb_2Se_3 absorber layers. Mater Sci Eng B 2024;303:117302. https://doi.org/10.1016/j.mseb.2024.117302.
[59] Dahmardeh Z, Saadat M. Exploring the potential of standalone and tandem solar cells with Sb_2S_3 and Sb_2Se_3 absorbers: a simulation study. Sci Rep 2023;13:22632. https://doi.org/10.1038/s41598-023-49269-w.
[60] Singh VK, Srivastava S, Singh AK, Chauhan MS, Patel SP, Singh RS. Theoretical study of highly efficient all-inorganic Sb_2S_3-on-Si monolithically integrated (2-T) and mechanically stacked (4-T) tandem solar cells using SCAPS-1D. Environ Sci Pollut Res 2023;30:98747–59. https://doi.org/10.1007/s11356-023-25292-2.

Marwa S. Salem was born in Gedda, KSA in 1979. She received her B.Sc. degree from Electronics and Communications engineering department, Faculty of engineering, Ain Shams University, Cairo Egypt in 2002. She owned her master's degree from the same university in the field of renewable energy in 2006. Also, she owned her Ph.D degree from the same university in the field of renewable energy especially in solar cells in 2013. She worked as a research assistant in Ain Shams University, faculty of engineering since 2003 till 2013. Currently, she is the Vice Dean of the Computer College, University Ha'il, Ha'il, Saudi Arabia. Her fields of research interests include VLSI design, MEMS technology, Nano technology, Renewable energy, Solar Cell, PV systems, Semiconductor physics, simulation and modelling of power devices.

Ahmed Shaker was born in Cairo, Egypt. He received the M.Sc. and Ph.D. degrees in 2003 and 2010, respectively, from Ain Shams University, Cairo, Egypt. He has been with Engineering Physics Department, Faculty of Engineering, Ain Shams University, since 1997, where he is currently a Professor of Engineering Physics. His fields of research include simulation and modeling of semiconductor power devices, solar cells, 3D detectors and nanoscale devices including TFETs and CNTFETs. Recently, he joined the Electrical and Computer Engineering (ECE) department, North Carolina State University (NCSU), Raleigh, USA, as a postdoctoral researcher where he is involved in solar cell and GaN-based LEDs fabrication and modeling.

Chao Chen received his Ph.D. from Huazhong University of Science and Technology in 2019. Now, he is a postdoctoral fellow at the Wuhan National Laboratory for Optoelectronics, Huazhong University of Science and Techno logy. His research interests are antimony chalcogenide thin-film solar cells and photodetectors.

Luying Li received her master's degree in 2006 in Physics Department of Wuhan University, and Ph.D. in 2011 in Physics Department of Ari zona State University. She started to work in Wuhan National Laboratory for Optoelectronics in Huazhong University of Science and Technology in Dec 2011. Her current research interest is about the relationship between atomic structures and specific physical properties of semiconductor nanomaterials, focusing on their electrostatic and in-situ properties at atomic resolution.

Mohamed Abouelatta was born in Cairo, Egypt. He received the B.Sc., M.Sc. degrees in 1996 and 2001, respectively, in Electronics and Communication engineering from Ain Shams University (ASU). He received PhD degrees from Ain Shams University and from the National Institute of Applied Sciences (INSA) of Lyon, France in 2010. He is now a Professor in the Faculty of Engineering, ASU. His fields of research are modeling, design, and characterization of Power devices, designing of Smart Power Integrated circuits, Nanodevices, Photovoltaic and 3D CMOS Heterogeneous Integrated Circuits.

Arwa N. Aledaily received the B.S. degree (Hons.) in information technology and the M.S. degree in computer science from King Saud University, Riyadh, Saudi Arabia, in 2007 and 2013, respectively. She is currently pursuing the Ph.D. degree in computer science, specializing in emotion recognition and brain–computer interface area. She worked as a Teacher Assistant and a Lecturer with King Saud University, from 2008 to 2014. She has been a Lecturer with the University of Hail, Hail, Saudi Arabia, since 2014. She is also enrolled in machine learning specialization from deeplearning.ai organization. Her research interests include brain–computer-interface, human–computer interaction, emotion recognition and applications of eye-tracking, EEG brain activity, and machine learning in general.

Walid Zein was born in Cairo, Egypt. He received the M.Sc. and Ph.D. degrees in 2002 and 2006, respectively, from Ain Shams University, Cairo, Egypt. He has been with the Engineering Physics Department, Faculty of Engineering, Ain Shams University, since 1997, where he is currently an Associate Professor of Engineering Physics. His fields of research include simulation and modeling of solar cells, photodetectors and nanoscale devices including TFETs and Carbon Nanotube FETs.

Mohamed Okil was born in Al Sharqia, Egypt in 1989. He received the M.Sc. and Ph.D. degrees in 2019 and 2023, respectively, from Benha University, Benha, Egypt. He has been with Basic Engineering Sciences Department, Benha Faculty of Engineering, Benha University, since 2013, where he is currently an Assistant Professor of Engineering Physics. His fields of research include Laser Spectroscopy, Materials Science, and Simulation and Modeling of Solar Cells.